A&A, 708, A86 (2026)
https://doi.org/10.1051/0004-6361/202558418

Astronomy & Astrophysics

Direct determination of the astrophysical reaction rate of ^{141}Pr(γ, n)^{140}Pr at the SSRF-SLEGS

J. H. Hu[1,2], Z. D. An[2,3,4,⋆], Z. R. Hao[5,⋆], Z. C. Li[6], G. T. Fan[5,⋆], H. W. Wang[5], Y. G. Ma[3,4,7], T. Liu[1,2], H. Liang[1,2], H. H. Wen[1], and C. C. Guo[1]

[1] Sino-French Institute of Nuclear Engineering and Technology, Sun Yat-sen University, Zhuhai 519082, China
[2] Institute of Modern Physics, Chinese Academy of Sciences, Lanzhou 730000, China
[3] Key Laboratory of Nuclear Physics and Ion-beam Application (MOE), Institute of Modern Physics, Department of Nuclear Science and Technology, Fudan University, Shanghai 200433, China
[4] Shanghai Research Center for Theoretical Nuclear Physics, NSFC and Fudan University, Shanghai 200438, China
[5] Shanghai Advanced Research Institute, Chinese Academy of Sciences, Shanghai 201210, China
[6] School of Nuclear Science and Technology, University of South China, Hengyang 421001, China
[7] School of Physics, East China Normal University, Shanghai 200241, China

Received 5 December 2025 / Accepted 27 February 2026

ABSTRACT

Context. The ^{141}Pr(γ, n) cross-section is critical to the nucleosynthesis of p-nuclides ^{136,138}Ce in thermonuclear supernovae and in massive stars. The photonuclear reaction of ^{141}Pr(γ, n) provides a new method for producing ^{140}Pr radioisotopes for positron emission tomography tracing in nuclear medicine.

Aims. We aim to perform an accurate measurement of the ^{141}Pr(γ, n)^{140}Pr cross-section over a sufficiently wide range of gamma energies of the p-process and deduce the ^{140}Pr(n, γ)^{141}Pr cross-section with γSF and TALYS-SMLO models. We determined the astrophysical reaction rate of ^{141}Pr(γ, n)^{140}Pr at the temperature range of 0.2–10 GK based on the new measurement cross-section of the ^{141}Pr(γ, n)^{140}Pr reaction.

Methods. We performed a new measurement of the ^{141}Pr photoneutron cross-section at the Shanghai Laser Electron Gamma Source of the Shanghai Synchrotron Radiation Facility using quasi-monoenergetic laser Compton scattered γ-ray beams. The neutrons emitted by the ^{141}Pr target were detected by the flat-efficiency detector array, while the γ beam transmitted by the ^{141}Pr target were attenuated by a copper absorber and then measured by a bismuth germanate detector in order to reconstruct the γ spectrum incident on the target.

Results. The cross-section data of ^{141}Pr(γ, n) were acquired using an unfolding iteration method with an uncertainty of less than 4%, and the inconsistencies between the available experimental data and evaluation libraries were discussed. The inverse reaction cross-section of ^{140}Pr(n, γ) and the reaction rates for the ^{141}Pr(γ, n) reaction were derived over the astrophysically relevant temperature range of the p-process nucleosynthesis model. The photodisintegration decay constants of the ^{141}Pr(γ, n) reaction for stellar temperatures between 0.2 GK and 10 GK are provided in a tabular form and by an analytical fitting expression. The $\lambda_{\gamma n}(^{141}\mathrm{Pr}) = 0.013 \pm 0.001\ \mathrm{s}^{-1}$ at a typical p-process temperature of $T = 2.5$ GK was also computed.

Conclusions. The photodisintegration decay constants of the ^{141}Pr(γ, n) reaction deviate significantly from previous theoretical predictions, and the uncertainties are significantly reduced in the direct measurement.

Key words. nuclear reactions, nucleosynthesis, abundances – stars: abundances

1. Introduction

The nucleosynthesis of heavy elements in stars is primarily driven by two neutron-capture processes: the slow (s) and the rapid (r) processes (Burbidge et al. 1957; Meyer 1994). However, the s and r processes cannot synthesise neutron-deficient stable nuclides in the mass range of $A \geq 74$ (from ^{74}Se to ^{196}Hg; Rauscher et al. 2016; Nishimura et al. 2018). These species are known as p-nuclides, where the p signifies their relatively high proton number compared to nearby normal and neutron-rich isotopes. The stellar process that produces p-nuclides is called the p-process. This process might include the (γ, n) reaction or the (p, γ) reaction (Arnould & Goriely 2003). The p-process requires an environment with an extreme temperature (2–3 GK), a condition typically found in thermonuclear supernovae (Burbidge et al. 1957).

Regarding p-nuclides, it has been proposed that they form via photodisintegration reactions involving pre-existing seed nuclei located in the outer shells of exploding massive stars (Rauscher et al. 2016). One possible mechanism for massive stars to acquire heavy s-process seed nuclei is via mass transfer in binary systems (Jorissen et al. 2016; Bisterzo et al. 2014). The observed barium stars and carbon-enhanced metal-poor stars with s-process enrichment (Pignatari et al. 2013) provide direct evidence of this process. Thermonuclear supernovae are another candidate site for p-nuclide production, and they arise from the explosion of a white dwarf that accretes mass from a companion star (Nishimura et al. 2018). This makes them ideal sites for p-process nucleosynthesis, particularly for bottleneck nuclides such as ^{141}Pr (Travaglio et al. 2014). These specific nuclides are produced during the explosive phase in layers enriched with seed nuclei formed via prior strong s-process nucleosynthesis (Yang et al. 2023). Fission also contributes to the production of p-nuclides. Roederer et al. (2023) indicated the existence of the

⋆ Corresponding authors: anzhendong@impcas.ac.cn; haozr@sari.ac.cn; fangt@sari.ac.cn

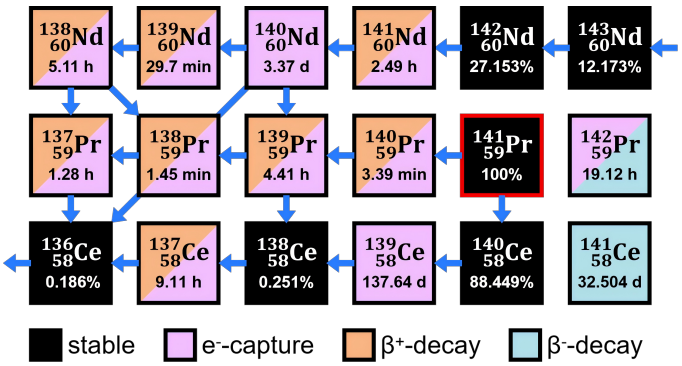

Fig. 1. Path of the *p*-process for core-collapse supernovae near ^{141}Pr.

fission fragments of transuranic (Z > 92) nuclei. Notably, the *p*-nuclides ^{96,98}Ru, ^{102}Pd, ^{156,158}Dy, ^{162}Er, ^{168}Yb, ^{174}Hf, ^{180}Ta, ^{184}Os, and ^{190}Pt may be produced by the fission of transuranic elements synthesised in the *r*-process.

The origin of Solar System *p*-nuclides (inferred from meteoritic and geological data) is elusive due to the lack of direct observational evidence. The low elemental abundance of *p*-nuclides prevents detection in stars or supernova remnants, and no element has a *p*-isotope as its dominant form. Thus, their nucleosynthesis must be investigated solely through theoretical models (Rauscher et al. 2016; Nishimura et al. 2018). Though uncertainties are introduced at each simulation step of a theoretical model, the initial uncertainties stem from the astrophysical reaction rates employed in the nuclear reaction networks (Yang et al. 2024). The ^{141}Pr(γ, n) cross-section is critical to the study of the *p*-process, particularly regarding the nucleosynthesis of *p*-nuclides ^{136,138}Ce, as shown in Fig. 1.

The unique electronic configurations of ^{140}Pr, with a 51% positron branch and a half-life of 3.39 min, make it essential in medical nuclear imaging and therapy. These characteristics also enable ^{140}Pr to play a key role in positron emission tomography tracing of pharmaceuticals (Severin et al. 2017). Its decay daughter is a stable nuclide, ^{140}Ce. Significantly, ^{140}Pr can be produced by bremsstrahlung photons in an electron linear accelerator. Thus, the cross-section of the ^{141}Pr(γ, n) reaction is a prerequisite for evaluating the economical efficiency of a ^{140}Pr generation method.

Previous experimental studies of the ^{141}Pr(γ, n) cross-section show discrepancies in the peak position and peak height of the giant dipole resonance (GDR; Zilges et al. 2022; Arnould & Goriely 2003). Cook et al. (1966) measured the ^{141}Pr(γ, n) cross-section based on bremsstrahlung photons from the Iowa State University synchrotron. This measurement resolved eleven resonances in the region below 20 MeV, with yield data taken at 0.125 MeV increments. By comparing the results of two different resolutions, we found that a better resolution would extend the peak height.

Sund et al. (1970) utilised a photon beam generated by the in-flight annihilation of positrons to perform their measurement. Sund's results are in good agreement with Cook's results in the energy regions below 14 MeV and above 16.26 MeV. Both measurements employed a NaI crystal detector. In the region between 14 MeV and 16.26 MeV, however, Sund's values are significantly lower, but Sund's results show good correspondence with the results of Bramblett et al. (1966). Both results show a smooth variation of the ^{141}Pr cross-section instead of dense resonances.

Beljaev & Semenov (1991) carried out a measurement based on betatron bremsstrahlung and a BF_3 detector. Utsunomiya et al. (2006) employed laser Compton scattering γ beams and ^{3}He proportional counters to measure the cross-section data. The systematic uncertainty was estimated to be between 5.8% and 7.2%. Their result, however, only covers the γ energy region of 9.5–12.4 MeV. Bholane et al. (2023) performed measurements using 10 and 15 MeV end point energy bremsstrahlung photons. Their results are underestimated compared with existing measurements and theoretical evaluations.

The Shanghai Laser Electron Gamma Source (SLEGS) is a γ-ray facility based on the inverse Compton scattering of 10.64 µm CO_2 laser photons from 3.5 GeV relativistic electrons from the storage ring of the Shanghai Synchrotron Radiation Facility (SSRF; Wang et al. 2022). As an energy-tunable laser Compton scattering γ-ray source, SLEGS provides γ beams with energies from 0.66 to 21 MeV in the slant-scattering mode at scattering angles of 20° to 160° and with a maximum energy of 21.7 MeV in the back scattering mode at 180° (Liu et al. 2024b). The energy of the beamline can be adjusted in slant-scattering mode with a minimum step of 10 keV.

In this study, the ^{141}Pr(γ, n) cross-sections were experimentally investigated by employing quasi-monochromatic and energy-tunable SLEGS γ-ray beams. In Sect. 2, a brief description of the experimental procedure utilised for the measurement of the ^{141}Pr(γ, n) cross-section is given. In Sect. 3 the results of the cross-section and the reaction rates in our experiment are presented, and the inconsistencies between the available experimental data and evaluated data are discussed. In Sect. 4 a general conclusion of this study is presented.

2. Experimental procedure

The experimental measurement was performed at the SSRF-SLEGS by applying the γ beams within the GDR energy range from the single-neutron separation energy (S_n = 9.40 MeV) to the double-neutron separation energy (S_{2n} = 17.33 MeV) of ^{141}Pr. The experimental setup for the photoneutron cross-section measurement is illustrated in Fig. 2. After passing through a coarse collimator (C5, 5 mm) and a three-hole collimator (T2, 2 mm), the γ beam irradiated a ^{141}Pr target (10 mm diameter, 5 mm thickness, 6.773 g/cm^3 density, and 99.95% purity) placed at the centre of a ^{3}He flat-efficiency detector (FED) array. The neutrons emitted by the ^{141}Pr target were detected by the FED array, while the γ beam transmitting the ^{141}Pr target were attenuated by a copper absorber and then measured by a bismuth germanate (BGO) detector in order to monitor the γ flux.

2.1. Detection of photoneutron with FED array

A calibrated array of 26 ^{3}He proportional counters embedded in a polyethylene moderator of 450 mm × 450 mm × 550 mm (Hao et al. 2020) was applied to detect the neutrons emitted by the photoneutron reaction (γ, n). These counters of the FED array were positioned in three concentric rings with radii of 6.5 cm, 11.0 cm, and 17.5 cm from the γ beam axis and were equipped with 1-inch diameter tubes in the inner ring and 2-inch diameter tubes in the middle and outer rings (Jiao et al. 2025). All the tubes were 0.5 cm long and filled with ^{3}He at 2 atm. The environmental background was shielded by a layer of 2 mm thick cadmium wrapped around the polyethylene. The bremsstrahlung background was subtracted by utilising a 50 µs laser duty cycle within a 1000 µs period. The neutron number (N_n) was obtained using the time-normalised background subtraction method (Hao et al. 2025b, 2026). The average neutron energy was acquired

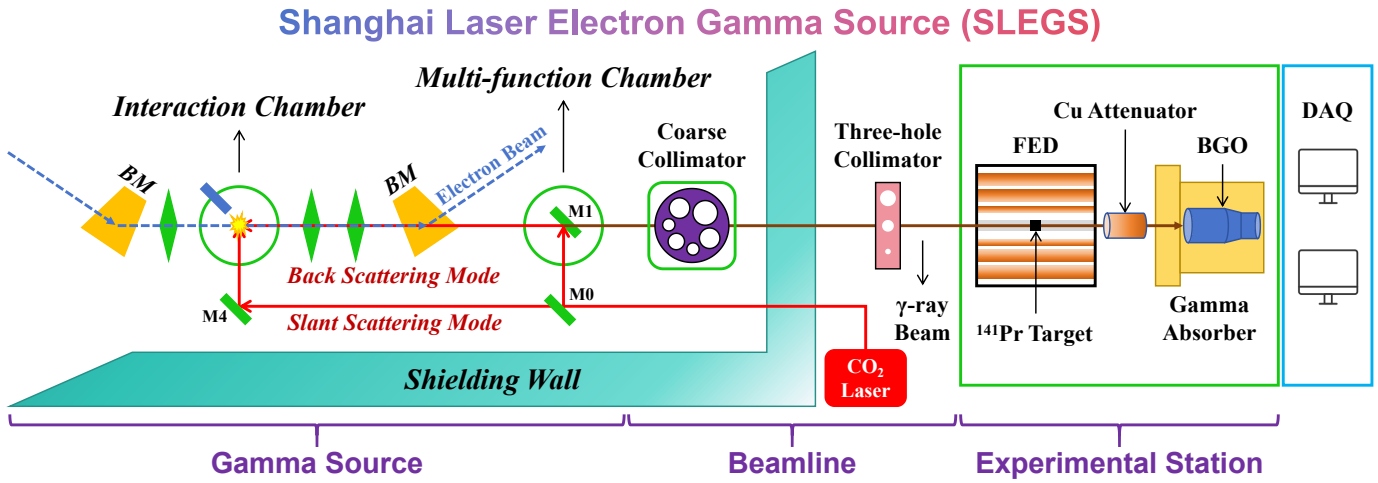

Fig. 2. Experimental setup for the (γ, n) cross-section measurement at SLEGS.

via the ring-ratio technique proposed by Berman et al. (1967); Berman & Fultz (1975), calibrated by a ^{252}Cf experiment and GEANT4-based efficiency curves (Hao et al. 2025a). The efficiency of the FED array is 42.10 ± 1.25%, corresponding to an average neutron energy of 2.13 MeV of ^{252}Cf. The detector's efficiency was high and nearly flat across the 1 keV–4 MeV neutron energy range typical for (γ, n) reactions, making it well suited for neutron detection.

2.2. Determination of the γ-ray spectrum with a BGO

A BGO detector of Φ76 mm × 200 mm was used to measure the γ-ray spectrum after copper attenuation. Its total-energy responses to monoenergetic γ-rays were characterised at the China Institute of Atomic Energy via (p, γ) reactions on LiF, ^{27}Al, and ^{13}C targets (Liu et al. 2024a). The γ-ray spectra measured at slant scattering angles (θ_{L}) of 95°, 103°, and 121° in this study are shown in Fig. 3a. To determine the γ-ray spectrum incident on the target, a direct unfolding technique was employed. This analysis was based on the BGO detector's response function, obtained via GEANT4 simulations (Liu et al. 2024a).

2.3. Data analysis

The experimental cross-section (folded cross-section) was determined by Eq. (1) (Jury et al. 1979; Filipescu et al. 2014):

$$\sigma_{\mathrm{exp}} = \int_{S_{\mathrm{n}}}^{E_{\mathrm{max}}} P(E_\gamma)\sigma(E_\gamma)\mathrm{d}(E_\gamma) = \frac{N_{\mathrm{n}}}{N_{\mathrm{t}} N_\gamma \xi \epsilon_{\mathrm{n}} g}, \quad (1)$$

where $P(E_\gamma)$ denotes the normalised distribution of the incident γ ray, N_{n} is the detected neutron number, N_γ is the number of incident γ photons, ϵ_{n} is the average neutron detection efficiency, N_{t} is the areal number density of target nuclei, ξ is the correction factor for a thick target, and g is the ratio of the gamma flux above S_{n}.

The experimental cross-section, σ_{exp}, is usually a convolution of the energy of the incident γ-beam, and it is caused by the broadening of the γ-ray energy distribution (Guttormsen et al. 1996). To de-convolute the unfolded cross-section, σ, from the measured experimental cross-section, an unfolding method was utilised based on Eq. (2) (Utsunomiya et al. 2018, 2024):

$$\sigma_{\mathrm{f}} = \mathbf{D}\sigma, \quad (2)$$

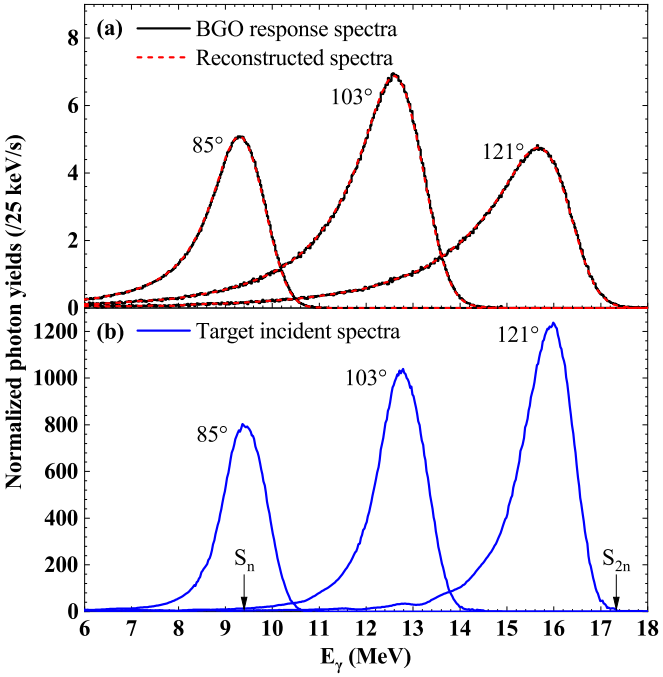

Fig. 3. (a) Typical spectra measured by the BGO detector (black line) and reconstructed from incident γ-ray spectra (dashed red line). (b) Corresponding γ spectra incident on the ^{141}Pr target.

where σ_{f} is the experimental cross-section folded with energy distribution $\mathbf{D}$, and σ is the unfolded cross-section to be determined. Equation (2) can be expressed in a matrix form:

$$\begin{bmatrix} \sigma_1 \\ \sigma_2 \\ \vdots \\ \sigma_N \end{bmatrix}_{\mathrm{f}} = \begin{bmatrix} D_{11} & D_{12} & \cdots & \cdots & D_{1M} \\ D_{21} & D_{22} & \cdots & \cdots & D_{2M} \\ \vdots & \vdots & \vdots & \vdots & \vdots \\ D_{N1} & D_{N2} & \cdots & \cdots & D_{NM} \end{bmatrix} \begin{bmatrix} \sigma_1 \\ \sigma_2 \\ \vdots \\ \sigma_M \end{bmatrix}. \quad (3)$$

Here, $N = 22$ and $M = 344$ represent the number of folded cross-sections and the energy bins of the γ spectrum, respectively. Each row of matrix $\mathbf{D}$ corresponds to a target incident spectrum, with only three of these spectral curves displayed in Fig. 3b as examples.

An initial vector of cross-section σ^0 was selected to start the iteration. It was then multiplied by **D** to obtain the zeroth folded vector: $\sigma_f^0 = \mathbf{D}\sigma^0$.

We set up the next trial input function σ^1 by adding the difference between σ_{exp} and σ_f^0 to σ^0:

$$\sigma^1 = \sigma^0 + (\sigma_{exp} - \sigma_f^0). \quad (4)$$

We iterated the above steps i times:

$$\sigma_f^i = \mathbf{D}\sigma^i, \quad (5)$$

$$\sigma^{i+1} = \sigma^i + (\sigma_{exp} - \sigma_f^i). \quad (6)$$

Once the convergence condition below was satisfied, the iteration came to an end:

$$\sigma_f^{i+1} \approx \sigma_{exp}. \quad (7)$$

3. Results and discussions

3.1. $^{141}Pr(\gamma, n)^{140}Pr$ reaction cross-section

The folded cross-section and the monochromatic (unfolded) cross-section of the $^{141}Pr(\gamma, n)^{140}Pr$ reaction obtained in this study, as well as their uncertainty, are illustrated in Fig. 4a and listed in Table A.1[1]. The present result has a systematic uncertainty of 3.17%, coming from the FED efficiency uncertainty of 3.02%, the BGO γ-spectrum uncertainty of 0.90%, and the target thickness uncertainty of 0.10%. The methodological uncertainty of this result is estimated to be about 2.05%, originating from the uncertainty of the neutron count algorithm of 2% and the uncertainty of the γ-spectrum unfolding method of 1%. Finally, the total uncertainty of this result is approximately 4%, except for the $(E_\gamma, \sigma(E_\gamma))$ pair of (9.57 MeV, 10.59 mb).

The present result is compared with previous studies in Figs. 4b and 5. Our result agrees well with previous values within the energy range of 9.5–13 MeV. In the region of 13–17 MeV, our result shows systematic deviation from other experimental values and the TALYS-based Evaluated Nuclear Data Library, 2023 version (TENDL-2023, Koning et al. 2019). The ratios of this result to the previous data are also shown in Fig. 5. In general, most of the ratios are distributed in the region of 0.5–1.5. This difference provides a new perspective for further theoretical calculation and experimental investigation.

According to the theoretical calculation of Belyaev et al. (1995), the peak value of the $^{141}Pr(\gamma, n)$ cross-section is about 450 mb. Moreover, the experimental result obtained by Cannington et al. (1968) indicates that the maximum cross-section at the main GDR peak at 15.45 MeV can be more than 500 mb. These findings support the reliability of our result to some extent.

The total cross-section integrated over the energy region of interest is defined as follows:

$$\sigma^{int} = \int_{E_{min}}^{E_{max}} \sigma(E_\gamma) dE_\gamma. \quad (8)$$

The systematic differences between two cross-section curves can be shown by their integral ratio $\sigma_1^{int}/\sigma_2^{int}$ (Varlamov et al. 2017). The integral ratios of this result in relation to the previous values, $\sigma_{SLEGS}^{int}/\sigma_{previous}^{int}$, are presented in Table 1. At the energy range of S_n-13 MeV, the integral ratios are between 0.96 and 1.16, showing good consistency. At the energy range of 13 MeV-S_{2n}, the integral ratios are distributed between 1.05 and 1.29, evidencing a slight deviation.

[1] The unfolded cross-section is also accessible via https://doi.org/10.57760/sciencedb.32822.

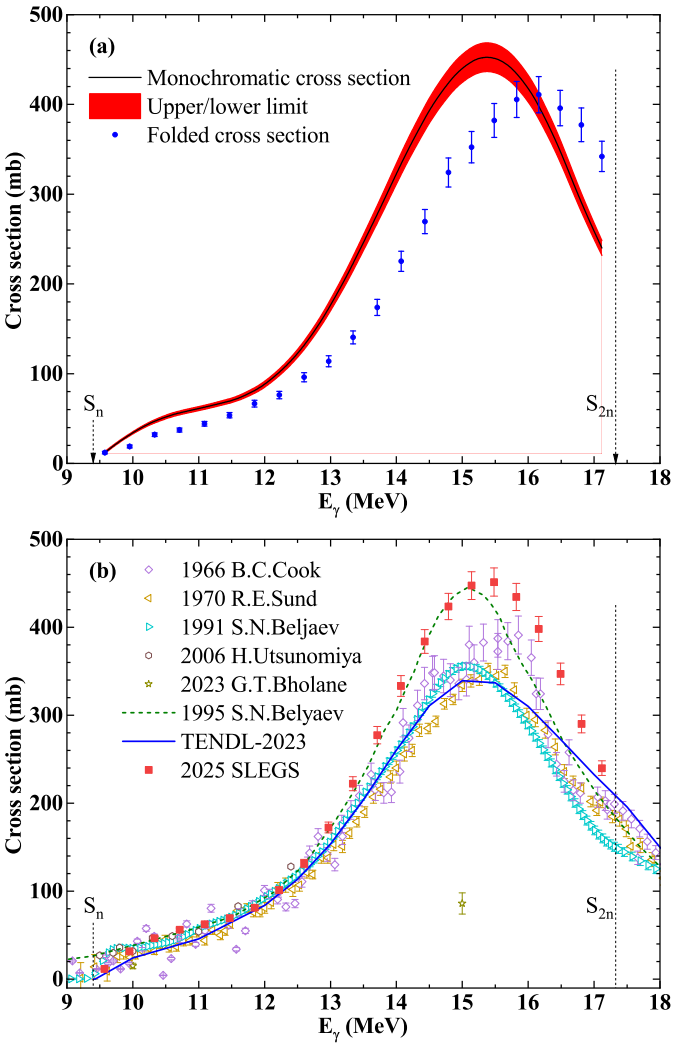

Fig. 4. (a) Reaction cross-section of $^{141}Pr(\gamma, n)$ as a function of the incident γ energy. The dots denote the folded cross-section, and the line with a shaded area is the monochromatic (unfolded) cross-section. (b) Comparison between this result of the cross-section and that of previous studies.

Table 1. Integral ratios of this result in relation to the previous values.

Source	$\sigma_{SLEGS}^{int}/\sigma_{previous}^{int}$	
	[S_n, 13 MeV]	[13 MeV, S_{2n}]
Koning et al. (2019) (TENDL-2023)	1.16	1.22
Belyaev et al. (1995)	0.96	1.05
Beljaev & Semenov (1991)	1.02	1.28
Sund et al. (1970)	1.14	1.29
Cook et al. (1966)	1.11	1.19

3.2. Radiative $^{140}Pr(n, \gamma)$ cross-section

The γ-ray strength function (γSF; Bartholomew et al. 1973; Kristiak & Betàk 2012) is a statistical quantity that describes compound nuclear reactions within the Hauser–Feshbach model. Its role in the de-excitation process enables the calculation of radiative (n, γ) cross-sections, which are crucial for the s-process nucleosynthesis of elements heavier than iron. According to

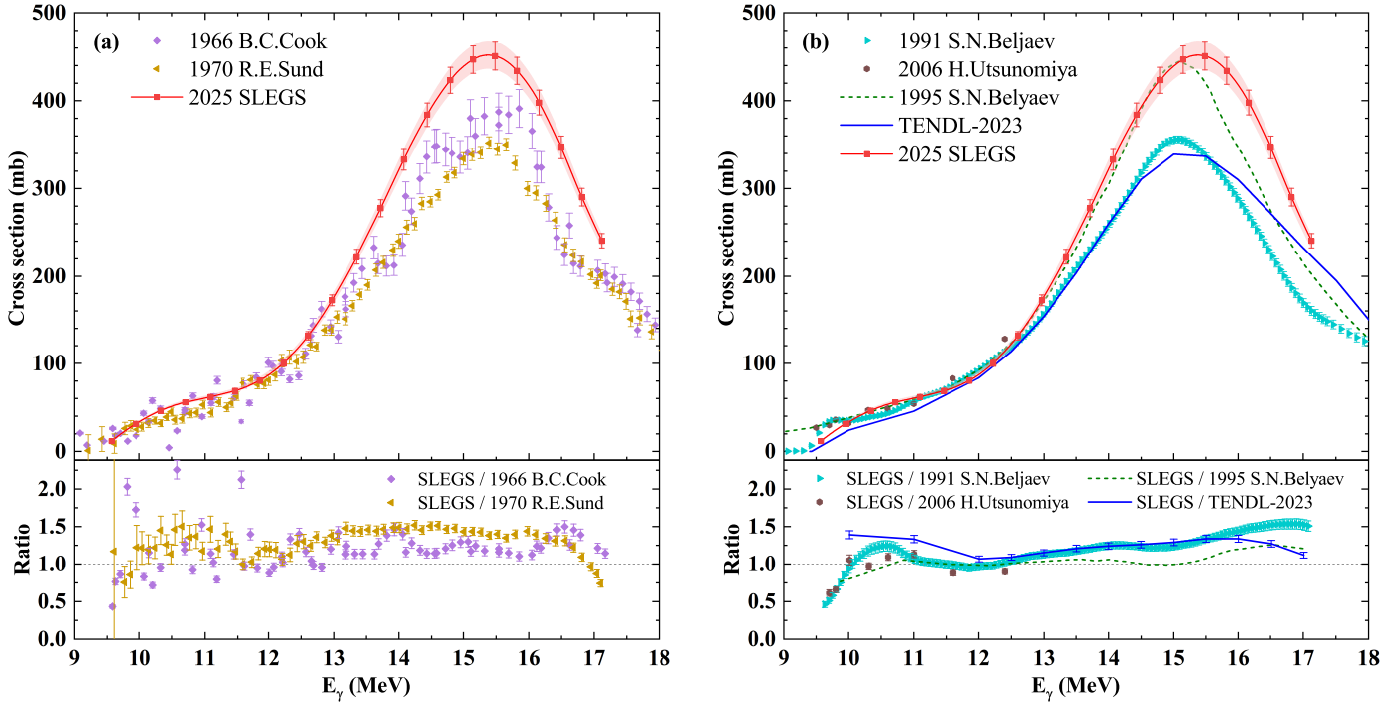

Fig. 5. Comparison of the present ^{141}Pr(γ, n) cross-section from SLEGS (dotted solid red line) with (a) the ^{141}Pr(γ, n) cross-section from Cook et al. (1966, purple rhombus) and Sund et al. (1970, yellow triangle), (b) the ^{141}Pr(γ, n) cross-section from Beljaev & Semenov (1991, cyan triangle), Utsunomiya et al. (2006, brown circle), Belyaev et al. (1995, dashed green line), and the ^{141}Pr(γ, n) cross-section from TENDL-2023 Koning et al. (2019, solid blue line).

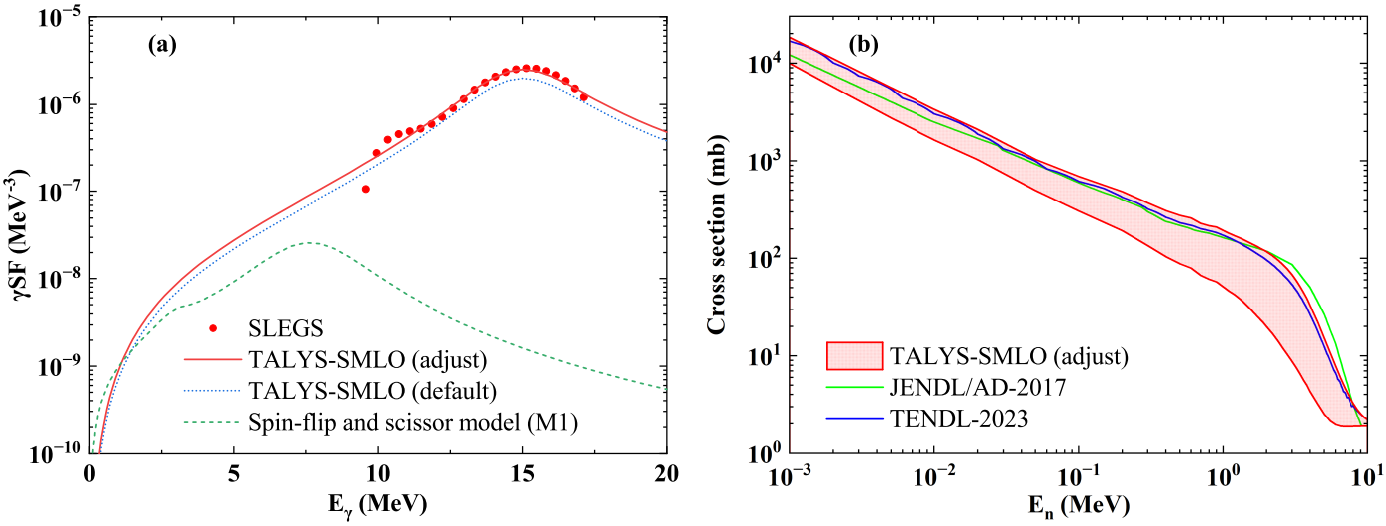

Fig. 6. (a) Comparison of the γSF of ^{141}Pr calculated using the default (dashed blue line) and adjusted (red line) SMLO models for the E1 strength in TALYS with the γSF extracted from our data (red dots). The spin-flip and scissor model for the M1 strength is indicated by the dashed green line. (b) Cross-section of ^{140}Pr(n, γ) calculated with the TALYS code based on the adjusted SMLO model.

the principle of detailed balance (Blatt & Weisskopf 1952) and the generalised Brink hypothesis, the equality of the upward and downward γSF $f_{\mathrm{X1}} = \overleftarrow{f_{\mathrm{X1}}} = \overrightarrow{f_{\mathrm{X1}}}$ gives the expression of the (downward) γSF with the (upward) (γ, n) cross-section $\sigma_{\gamma\mathrm{n}}$ through Eq. (9) (Capote et al. 2009):

$$f_{\mathrm{X1}}(E_\gamma) = \frac{1}{g_J \pi^2 \hbar^2 c^2} \frac{\sigma_{\gamma\mathrm{n}}(E_\gamma)}{E_\gamma}. \quad (9)$$

Here, X is either electric (E) or magnetic (M). The spin factor $g_J = (2J + 1)/(2J_0 + 1)$ (Zilges et al. 2022), where $J = 1$ and $J_0 = 0$ (ground state), and $1/g_J\pi^2\hbar^2c^2 = 8.674 \times 10^{-8}$ mb^{-1}MeV^{-2}. This relation yields the experimentally constrained γSF from the measured ^{141}Pr(γ, n) reaction data, as indicated by the red dots in Fig. 6a.

The TALYS code (v1.96; Koning & Rochman 2012; Koning et al. 2023) incorporates various phenomenological and microscopic models to describe the γSF. The default and adjusted simple modified Lorentzian (SMLO) models (Goriely & Plujko 2019) for the E1 strength closely approximate the experimental values. The dotted red and blue lines in Fig. 6a represent the γSFs calculated using the SMLO models. The dashed green line

in Fig. 6a illustrates the spin-flip and scissor model of the M1 strength (Balbutsev et al. 2011).

The radiative (n, γ) cross-section is dependent on the γSF and highly sensitive to the choice of the nuclear level density model (Li et al. 2023). The radiative ^{140}Pr(n, γ) cross-section was calculated based on the adjusted SMLO model (Li et al. 2025). The results are presented in Fig. 6b with the red band. The spin-flip and scissor model of the M1 strength was considered in the TALYS calculations. The theoretical uncertainty corresponds to the employment of six nuclear level density models (Koning et al. 2023). In Fig. 6b, our results are compared with JENDL/AD-2017 and TENDL-2023 evaluations. We observed good agreement between our results and each of the evaluation curves. To the best of our knowledge, this work provides the first experimentally constrained cross-section for the ^{140}Pr(n, γ) reaction. This result thereby provides direct support for the principle of detailed balance and the generalised Brink hypothesis in the case of the ^{141}Pr isotope.

3.3. Photodisintegration decay constant

The reaction rate of a photo-induced reaction (number of reactions per time and per unit volume) can also be called a photodisintegration rate. If we divide the photodisintegration rate by the target nucleus density (particles per volume), we obtain a decay constant (probability of decay per nucleus per second). The decay constant of a (γ, n) reaction can be determined with Eq. (10):

$$\lambda_{\gamma n} = \frac{r_{\gamma n}}{N} = \int_{S_n}^{S_{2n}} cC_\gamma(E_\gamma)\sigma(E_\gamma)\mathrm{d}E_\gamma, \tag{10}$$

with $r_{\gamma n}$ as the photodisintegration rate, N as the target nucleus density, c as the speed of light, and $C_\gamma(E_\gamma)$ as the number of photons with energy E_γ. The calculation shows that the cross-section above S_{2n} contributes negligibly to the integral, as the photon number decreases rapidly. This validates our choice of integration region. In this study, we find $\lambda_{\gamma n}(^{141}\mathrm{Pr}) = 0.013 \pm 0.001\,\mathrm{s}^{-1}$ at a typical p-process temperature of $T = 2.5$ GK, which agrees with the value ($0.015 \pm 0.004\ \mathrm{s}^{-1}$) of Utsunomiya et al. (2006) within the respective uncertainties, as shown in Fig. 7a. The uncertainty in our result is an improvement over that of Utsunomiya et al. (2006). In Table B.1 we compare the photodisintegration decay constants for stellar temperatures between 0.2 GK and 10 GK obtained in this work with values from previous studies[2].

The $\lambda_{\gamma n}$ ratios of the previous values in relation to the SLEGS results, $\lambda_{\gamma n}^{\mathrm{previous}}/\lambda_{\gamma n}^{\mathrm{SLEGS}}$, at the temperature range of 0.2–10 GK are illustrated in Fig. 7b. Overall, the $\lambda_{\gamma n}(^{141}\mathrm{Pr})$ obtained in this work are lower than those reported by Belyaev et al. (1995) at the entire range and Utsunomiya et al. (2006) above 0.9 MeV. However, they are higher than those from TENDL-2023 (Koning et al. 2019), and compared to those from Rauscher & Thielemann (2000), they are lower below 4.5 MeV and higher above 4.5 MeV. This work obtained an experimental ^{141}Pr(γ, n)^{140}Pr reaction cross-section at the energy range of S_n to S_{2n}. The broad energy coverage provides high-precision input, ensuring a more accurate calculation of the $\lambda_{\gamma n}(^{141}\mathrm{Pr})$. The present $\lambda_{\gamma n}$ deviate significantly from previous theoretical predictions, and the uncertainties are significantly reduced.

[2] The photodisintegration decay constants are also accessible via https://doi.org/10.57760/sciencedb.32822.

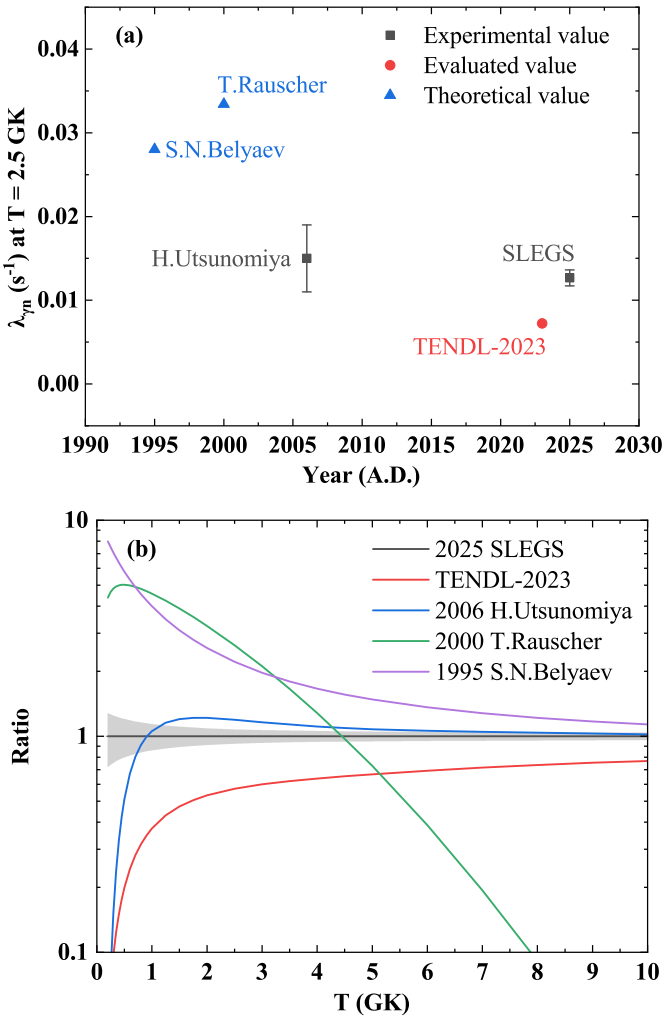

Fig. 7. (a) Comparison of $\lambda_{\gamma n}$ at $T = 2.5$ GK. (b) Ratios of $\lambda_{\gamma n}$ of the previous values in relation to the SLEGS results ($\lambda_{\gamma n}^{\mathrm{previous}}/\lambda_{\gamma n}^{\mathrm{SLEGS}}$) for the ^{141}Pr($\gamma$, n) reaction.

A common form of the reaction rate is an analytical formula with an appropriate parametrization for applications in the p-process of stellar models. We used the standard form of the JINA Reaclib Database (Cyburt et al. 2010) to fit $\lambda_{\gamma n}(^{141}\mathrm{Pr})$ as a function of T_9 (GK) and obtained $a = [a_0, a_1, a_2, a_3, a_4, a_5, a_6]$ in Eq. (11):

$$\lambda_{\gamma n} = \exp(a_0 + a_1/T_9 + a_2/T_9^{1/3} + a_3T_9^{1/3} + a_4T_9 + a_5T_9^{5/3} + a_6\log(T_9)). \tag{11}$$

The fitting results we obtained show that a = [57.09, 157.9, -5263, 5253, -194.9, 7.284, -3173], with $R^2 = 0.9999$.

4. Conclusion

We performed new measurements on the cross-section of the ^{141}Pr(γ, n) cross-section in the energy range S_n to S_{2n} by applying quasi-monoenergetic γ beams at SLEGS. Based on the unfolding iteration method, the unfolded cross-section data were acquired within the energy region of 9.57–17.12 MeV, with a total uncertainty of approximately 3.9%. The present result demonstrates good consistency with previous values at the energy range of S_n-13 MeV and a slight discrepancy at the energy range

of 13 MeV-S_{2n}. We determined the radiative ^{140}Pr(n, γ) cross-section using the adjusted SMLO model for the E1 strength in TALYS with the γSF extracted from our data. The photodisintegration decay constant at the temperature range of 0.2–10 GK was computed and compared to the results of previous studies.

This result will provide key data for the study of the p-process, particularly the nucleosynthesis of p-nuclides ^{136,138}Ce. The implications of the newly determined ^{141}Pr(γ, n) cross-sections for the abundances of the p-nuclei ^{136,138}Ce can be qualitatively assessed based on the findings of Rayet et al. (1990) and Käppeler et al. (1996). A future study may be carried out to see if the present data would ameliorate the isotope pattern in the calculations of Prantzos et al. (1990), together with the ^{136,138}Ce(n, γ) cross-section measured by Sahoo et al. (2024). Furthermore, the new result will contribute to the production of medical isotopes via accelerator, such as ^{140}Pr. Further investigation will be conducted to extend the measurement range to above S_{2n}, advance the theoretical understanding of newly observed resonance states, and facilitate the direct application of the findings to stellar evolution modelling and nuclear technology systems.

Acknowledgements. We thank the BL03SSID of the SSRF (https://cstr.cn/31124.02.SSRF.BL03SSID) for the assistance on measurements and analysis. This work was supported by the National Natural Science Foundation of China (Grant Nos. 12475152, 12147101, U1832182, and U2032137), and the Natural Science Foundation of Guangdong Province, China (Grant No. 2022A1515011184).

References

Arnould, M., & Goriely, S. 2003, Phys. Rep., 384, 1
Balbutsev, E., Molodtsova, I., & Schuck, P. 2011, Nucl. Phys. A, 872
Bartholomew, G. A., Earle, E. D., Ferguson, A. J., Knowles, J. W., & Lone, M. A. 1973, in Advances in Nuclear Physics, 7, eds. M. Baranger, & E. Vogt (Boston, MA: Springer US), 229
Beljaev, S. N., & Semenov, V. A. 1991, Izv. Akad. Nauk SSSR, 155, 55
Belyaev, S. N., Vasil'ev, O. V., Nechkin, A. A., et al. 1995, The structure of the (γ, n) cross section in ^{141}Pr, Tech. rep.
Berman, B. L., & Fultz, S. C. 1975, Rev. Mod. Phys., 47, 713
Berman, B. L., Caldwell, J. T., Harvey, R. R., et al. 1967, Phys. Rev., 162, 1098
Bholane, G. T., Ganesapandy, T. S., Patil, S. H., et al. 2023, Eur. Phys. J. A, 59, 127
Bisterzo, S., Travaglio, C., Gallino, R., Wiescher, M., & Käppeler, F. 2014, ApJ, 787, 10
Blatt, J. M., & Weisskopf, V. F. 1952, Theoretical Nuclear Physics (New York: Wiley)
Bramblett, R., Caldwell, J., Berman, B., Harvey, R., & Fultz, S. 1966, Phys. Rev., 148, 1198
Burbidge, E. M., Burbidge, G. R., Fowler, W. A., & Hoyle, F. 1957, Rev. Mod. Phys., 29, 547
Cannington, P. H., Stewart, R. J. J., Spicer, B. M., & Huber, M. G. 1968, Nucl. Phys. A, 109, 385
Capote, R., Herman, M., Obložinský, P., et al. 2009, Nucl. Data Sheets, 110, 3107
Cook, B. C., Hutchinson, D. R., Waring, R. C., et al. 1966, Phys. Rev., 143, 730
Cyburt, R. H., Amthor, A. M., Ferguson, R., et al. 2010, ApJS, 189, 240
Filipescu, D. M., Gheorghe, I., Utsunomiya, H., et al. 2014, Phys. Rev. C, 90, 064616
Goriely, S., & Plujko, V. 2019, Phys. Rev. C, 99, 014303
Guttormsen, M., Tveter, T. S., Bergholt, L., Ingebretsen, F., & Rekstad, J. 1996, Nucl. Instrum. Methods Phys. Res., Sect. A, 374, 371
Hao, Z. R., Fan, G. T., Liu, L. X., et al. 2020, Nucl. Tech., 43, 110501
Hao, Z. R., Fan, G. T., Wang, H. W., et al. 2025a, Sci. Bull., 70, 2591
Hao, Z. R., Liu, L. X., Zhang, Y., et al. 2025b, Nucl. Sci. Tech., 36, 183
Hao, Z. R., Liu, L., Wang, H. W., et al. 2026, Nucl. Instrum. Methods Phys. Res., Sect. A, 1082, 171026
Jiao, P., Hao, Z. R., Sun, Q. K., et al. 2025, Nucl. Sci. Tech., 36, 66
Jorissen, A., Van Eck, S., Van Winckel, H., et al. 2016, A&A, 586, A158
Jury, J. W., Berman, B. L., Faul, D. D., et al. 1979, Phys. Rev. C, 19, 1684
Koning, A. J., & Rochman, D. 2012, Nucl. Data Sheets, 113, 2841
Koning, A. J., Rochman, D., Sublet, J.-C., et al. 2019, Nucl. Data Sheets, 155, 1
Koning, A., Hilaire, S., & Goriely, S. 2023, Eur. Phys. J. A, 59, 131
Kristiak, J., & Betàk, E. 2012, Neutron Induced Reactions: Proceedings of the 4th International Symposium Smolenice, Czechoslovakia, June 1985 (Springer Science & Business Media)
Käppeler, F., Toukan, K. A., Schumann, M., & Mengoni, A. 1996, Phys. Rev. C, 53, 1397
Li, X. K., An, Z. D., Jiang, W., et al. 2023, Phys. Rev. C, 108, 035802
Li, Z. C., Hao, Z. R., Sun, Q. K., et al. 2025, Nucl. Sci. Tech., 36, 34
Liu, L. X., Utsunomiya, H., Fan, G. T., et al. 2024a, Nucl. Instrum. Methods Phys. Res., Sect. A, 1063, 169314
Liu, L. X., Wang, H. W., Fan, G. T., et al. 2024b, Nucl. Sci. Tech., 35, 111
Meyer, B. S. 1994, ARA&A, 32, 153
Nishimura, N., Rauscher, T., Hirschi, R., et al. 2018, MNRAS, 474, 3133
Pignatari, M., Zinner, E., Bertolli, M. G., et al. 2013, ApJ, 771, L7
Prantzos, N., Hashimoto, M., Rayet, M., & Arnould, M. 1990, A&A, 238, 455
Rauscher, T., & Thielemann, F.-K. 2000, ADNDT, 75, 1
Rauscher, T., Nishimura, N., Hirschi, R., et al. 2016, MNRAS, 463, 4153
Rayet, M., Arnould, M., & Prantzos, N. 1990, A&A, 227, 271
Roederer, I. U., Vassh, N., Holmbeck, E. M., et al. 2023, Science, 382, 1177
Sahoo, R. N., Paul, M., Kashiv, Y., et al. 2024, Phys. Rev. C, 109, 025808
Severin, G. W., Kristensen, L. K., Nielsen, C. H., et al. 2017, Front. Med., 4, 98
Sund, R. E., Verbinski, V. V., Weber, H., & Kull, L. A. 1970, Phys. Rev. C, 2, 1129
Travaglio, C., Gallino, R., Rauscher, T., et al. 2014, ApJ, 795, 141
Utsunomiya, H., Makinaga, A., Goko, S., et al. 2006, Phys. Rev. C, 74, 025806
Utsunomiya, H., Renstrøm, T., Tveten, G. M., et al. 2018, Phys. Rev. C, 98, 054619
Utsunomiya, H., Goriely, S., Kimura, M., et al. 2024, Phys. Rev. C, 109, 014617
Varlamov, V., Ishkhanov, B., & Orlin, V. 2017, Phys. Rev. C, 95, 054607
Wang, H. W., Fan, G. T., Liu, L. X., et al. 2022, Nucl. Sci. Tech., 33, 87
Yang, G. L., An, Z. D., Jiang, W., et al. 2023, Nucl. Sci. Tech., 34, 1
Yang, G. L., An, Z. D., Jiang, W., et al. 2024, Phys. Rev. Res., 6, 013225
Zilges, A., Balabanski, D., Isaak, J., & Pietralla, N. 2022, Prog. Part. Nucl. Phys., 122, 103903

Appendix A: ^{141}Pr(γ, n)^{140}Pr cross-section

Table A.1 shows the unfolded ^{141}Pr(γ, n)^{140}Pr cross-section as well as its corresponding uncertainties.

Table A.1. Unfolded cross-section and corresponding uncertainties for ^{141}Pr(γ, n)^{140}Pr.

Photon energy (MeV)	Cross-section (mb)	Statistical uncertainty (mb)	Methodological uncertainty (mb)	Systematical uncertainty (mb)	Total uncertainty (mb)
9.57	11.66	0.93	0.22	0.37	1.02
9.95	31.65	0.31	0.65	1.00	1.23
10.33	46.71	0.21	0.87	1.47	1.72
10.71	56.24	0.31	0.97	1.77	2.04
11.09	62.55	0.46	1.04	1.97	2.27
11.47	69.50	0.56	1.15	2.19	2.54
11.85	81.24	0.60	1.35	2.56	2.96
12.22	101.23	0.59	1.69	3.19	3.66
12.60	131.54	0.57	2.18	4.15	4.72
12.97	172.44	0.56	2.82	5.44	6.15
13.34	222.22	0.58	3.58	7.01	7.89
13.71	277.46	0.64	4.41	8.75	9.82
14.07	333.26	0.73	5.25	10.51	11.77
14.43	383.94	0.82	6.04	12.10	13.55
14.79	423.69	0.88	6.69	13.36	14.97
15.14	447.40	0.88	7.13	14.10	15.82
15.48	451.44	0.82	7.30	14.23	16.01
15.82	434.46	0.70	7.14	13.70	15.46
16.16	397.99	0.56	6.63	12.55	14.20
16.49	347.01	0.49	5.76	10.94	12.37
16.81	290.17	0.62	4.52	9.15	10.22
17.12	239.93	1.15	2.98	7.56	8.21

Appendix B: Photodisintegration decay constant

Table B.1 presents the photodisintegration decay constant $\lambda_{\gamma n}$ of ^{141}Pr calculated in this work as a function of T_9, compared with values from previous studies.

Table B.1. Photodisintegration decay constant of ^{141}Pr determined in this work compared with values from previous studies.

T_9	$\lambda_{\gamma n}$ (s^{-1}) from 2025 SLEGS			$\lambda_{\gamma n}$ (s^{-1}) from			
(GK)	Low	Median	High	Utsunomiya	Belyaev	TENDL-2023	Rauscher
0.20	2.67E-222	3.70E-222	4.72E-222	1.11E-223	2.95E-221	1.68E-223	1.62E-221
0.25	8.15E-175	1.10E-174	1.39E-174	8.83E-176	8.27E-174	7.77E-176	5.13E-174
0.30	3.91E-143	5.18E-143	6.45E-143	7.87E-144	3.66E-142	5.03E-144	2.50E-142
0.35	1.73E-120	2.26E-120	2.78E-120	5.36E-121	1.51E-119	2.79E-121	1.11E-119
0.40	1.73E-103	2.22E-103	2.70E-103	7.30E-104	1.41E-102	3.32E-104	1.11E-102
0.45	2.95E-90	3.73E-90	4.52E-90	1.57E-90	2.26E-89	6.53E-91	1.88E-89
0.50	1.16E-79	1.45E-79	1.74E-79	7.40E-80	8.39E-79	2.88E-80	7.30E-79
0.60	9.47E-64	1.16E-63	1.37E-63	7.78E-64	6.15E-63	2.82E-64	5.79E-63
0.70	2.30E-52	2.77E-52	3.24E-52	2.22E-52	1.36E-51	7.80E-53	1.36E-51
0.80	8.24E-44	9.78E-44	1.13E-43	8.89E-44	4.46E-43	3.09E-44	4.71E-43
0.90	3.81E-37	4.47E-37	5.13E-37	4.44E-37	1.90E-36	1.55E-37	2.10E-36
1.00	8.38E-32	9.71E-32	1.11E-31	1.03E-31	3.89E-31	3.63E-32	4.44E-31
1.25	3.69E-22	4.19E-22	4.69E-22	4.85E-22	1.46E-21	1.80E-22	1.78E-21
1.50	1.06E-15	1.19E-15	1.31E-15	1.43E-15	3.68E-15	5.61E-16	4.63E-15
1.75	4.57E-11	5.05E-11	5.54E-11	6.15E-11	1.41E-10	2.56E-11	1.80E-10
2.00	1.41E-07	1.55E-07	1.69E-07	1.88E-07	3.97E-07	8.26E-08	5.02E-07
2.50	1.17E-02	1.27E-02	1.36E-02	1.51E-02	2.80E-02	7.24E-03	3.34E-02
3.00	2.37E+01	2.55E+01	2.72E+01	2.96E+01	5.01E+01	1.52E+01	5.37E+01
3.50	5.72E+03	6.09E+03	6.47E+03	6.91E+03	1.09E+04	3.78E+03	1.01E+04
4.00	3.62E+05	3.84E+05	4.06E+05	4.26E+05	6.38E+05	2.44E+05	4.92E+05
4.50	9.35E+06	9.89E+06	1.04E+07	1.08E+07	1.54E+07	6.45E+06	9.63E+06
5.00	1.29E+08	1.36E+08	1.43E+08	1.47E+08	2.01E+08	9.06E+07	9.91E+07
6.00	6.97E+09	7.32E+09	7.67E+09	7.75E+09	9.96E+09	5.07E+09	2.84E+09
7.00	1.27E+11	1.34E+11	1.40E+11	1.40E+11	1.71E+11	9.56E+10	2.59E+10
8.00	1.18E+12	1.24E+12	1.29E+12	1.29E+12	1.51E+12	9.12E+11	1.13E+11
9.00	6.99E+12	7.30E+12	7.60E+12	7.52E+12	8.54E+12	5.50E+12	2.97E+11
10.00	2.99E+13	3.12E+13	3.25E+13	3.18E+13	3.54E+13	2.40E+13	5.39E+11